Title

Physical basis for distinct basal and mechanically gated activity of the human K+ channel TRAAK

Journal

Neuron, 109(18)

ISSN

0896-6273

Authors

Rietmeijer, Robert A
Sorum, Ben
Li, Baobin
et al.

Publication Date

2021-09-01

DOI

10.1016/j.neuron.2021.07.009

Peer reviewed

HHS Public Access

Author manuscript

Neuron. Author manuscript; available in PMC 2022 September 15.

Published in final edited form as:

Neuron. 2021 September 15; 109(18): 2902–2913.e4. doi:10.1016/j.neuron.2021.07.009.

Physical basis for distinct basal and mechanically-gated activity of the human K+ channel TRAAK

Robert A. Rietmeijer[1,2,3,4,#], **Ben Sorum**[1,2,4,#], **Baobin Li**[1,2,4], **Stephen G. Brohawn**[1,2,4,5,*]

[1]Department of Molecular & Cell Biology, University of California Berkeley, Berkeley, California 94720, USA

[2]Helen Wills Neuroscience Institute, University of California Berkeley, Berkeley, California 94720, USA

[3]Biophysics Graduate Program, University of California Berkeley, Berkeley, California 94720, USA

[4]California Institute for Quantitative Biology (QB3), University of California, Berkeley, CA 94720, USA

[5]Corresponding author and lead contact

Summary

TRAAK is a mechanosensitive two-pore domain K^+ (K2P) channel localized to nodes of Ranvier in myelinated neurons. TRAAK deletion in mice results in mechanical and thermal allodynia and gain-of-function mutations cause the human neurodevelopmental disorder FHEIG. TRAAK displays basal and stimulus-gated activities typical of K2Ps, but the mechanistic and structural differences between these modes are unknown. Here, we demonstrate that basal and mechanically-gated openings are distinguished by their conductance, kinetics, and structure. Basal openings are low conductance, short duration, and due to a conductive channel conformation with the interior cavity exposed to the surrounding membrane. Mechanically-gated openings are high conductance, long duration, and due to a channel conformation in which the interior cavity is sealed to the surrounding membrane. Our results explain how dual modes of activity are produced by a single ion channel and provide a basis for the development of state-selective pharmacology with the potential to treat disease.

Graphical Abstract

*Correspondence: brohawn@berkeley.edu.
#These authors contributed equally

Author Contributions

S.G.B., R.A.R., and B.S. conceived of the project, analyzed data, and wrote the manuscript. R.A.R. performed all aspects of the biochemistry and structural biology. B.S. performed all aspects of the electrophysiology. R.A.R. and B.S. generated constructs for recording. B.L. cultured the hybridoma for antibody purification. S.G.B. supervised the project and secured funding.

Declaration of Interests

The authors declare no competing interests.

Inclusion and Diversity

While citing references scientifically relevant for this work, we also actively worked to promote gender balance in our reference list.

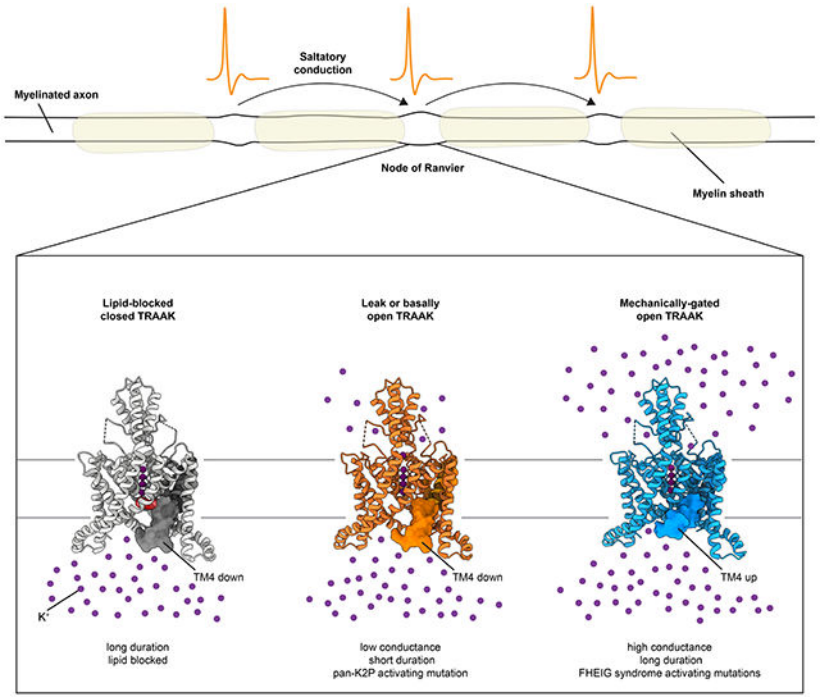

eTOC blurb

The K2P-type ion channel TRAAK involved in action potential propagation generates leak currents and is further activated by mechanical force. Rietmeijer, Sorum et al. study TRAAK gain-of-function mutations including those that cause the human neurodevelopmental FHEIG syndrome and show leak and mechanically-gated openings have distinct structures and electrical properties.

Introduction

Two-pore domain K^+ (K2P) channels display low basal activity (also referred to as leak, background, fluxgated, or resting activity) that is important for setting and maintaining the resting membrane potential in many cells (Enyedi and Czirják, 2010; Renigunta et al., 2015). In addition, K2Ps are further activated by diverse physical and chemical stimuli including membrane tension, temperature, voltage, pH, signaling lipids, and calcium to regulate cellular electrical excitability. K2Ps are physiologically relevant targets of volatile anesthetics and antidepressants and their dysregulation has been implicated in pathologies including migraine, depression, pulmonary hypertension, atrial fibrillation, diabetes mellitus, Birk-Barel syndrome, and FHEIG syndrome (Facial Dysmorphism, Hypertrichosis, Epilepsy, Intellectual disability, and Gingival outgrowth) (Enyedi and Czirják, 2010; Barel et al., 2008; Bauer et al., 2018; Heurteaux et al., 2006; Lafrenière et al., 2010; Ma et al., 2013; Royal et al., 2019; Schmidt et al., 2015; Vierra et al., 2015).

TRAAK is a mechanosensitive K2P expressed in the nervous system of jawed vertebrates and localized to nodes of Ranvier, the gaps in myelinated axons where the action potential is regenerated during saltatory conduction(Brohawn et al., 2019; Kanda et al.,

2019; Maingret et al., 1999). TRAAK accounts for ~25% of nodal background K^+ conductance and maintains the resting membrane potential and voltage gated-Na^+ channel availability required for high frequency spiking (Brohawn et al., 2019; Kanda et al., 2019)). Altering TRAAK activity in animals has physiological consequences; TRAAK knockout mice display mechanical and thermal allodynia and mechanical hyperalgesia while gain-of-function mutations in humans ($TRAAK_{A198E}$ and $TRAAK_{A270P}$) underlie the neurodevelopmental disorder FHEIG (Bauer et al., 2018; Noël et al., 2009).

TRAAK basal activity can be activated ~100-fold by increased membrane tension (Brohawn et al., 2014a, 2014b; Sorum et al., 2021). A model for mechanical gating primarily involves conformational changes in transmembrane helix 4 (TM4) (Brohawn et al., 2014b). In this model, nonconductive (closed) TRAAK adopts a TM4 “down” conformation and conductive (open) TRAAK adopts a TM4 “up” conformation. When TM4 is down, a lipid acyl chain can enter the channel cavity below the selectivity filter through membrane facing openings and sterically block the conduction path. Movement of TM4 up seals the membrane facing openings, prevents lipid access, and permits ion conduction. Structures of these two conformations provide a biophysical explanation for mechanosensitivity: shape changes upon opening, including an expansion in cross sectional area and increase in cylindricity, are energetically favored by membrane tension.

Notably, single channel recordings of TRAAK, and the closely related mechanosensitive K2P channels TREK1 and TREK2, suggest the presence of multiple distinct open and closed states (Bang et al., 2000; Kang et al., 2005; Maingret et al., 1999; Patel et al., 1998; Sorum et al., 2021; Xian Tao Li et al., 2006). In addition, alternative models for gating K2Ps posit closures involving C-type gating at the selectivity filter (Bagriantsev et al., 2011; Chatelain et al., 2012; Cohen et al., 2008; Li et al., 2020; Lolicato et al., 2020; Niemeyer et al., 2010; Piechotta et al., 2011; Sandoz et al., 2009; Schewe et al., 2016), closures involving dewetting of the channel cavity (Aryal et al., 2014, 2015), and openings that do not involve upward movement of TM4 (Lolicato et al., 2014; McClenaghan et al., 2016). For TRAAK, and other K2Ps, basally open and stimulus-activated currents display different voltage dependence (Schewe et al., 2016), consistent with structurally distinct open states. Here, we show basal and mechanically-gated TRAAK open states are distinct in their conductance, kinetics, and structure and present a model for channel gating that associates conformational and functional states.

Results

Basal and mechanically-gated TRAAK openings are physically distinct

A macroscopic recording from a patch containing wild-type TRAAK ($TRAAK_{WT}$) illustrates basal activity and robust activation by membrane tension (generated by negative pressure applied through the patch pipette) that are characteristic of the channel (Fig. 1A,B). We performed single channel recordings to determine whether basally open and mechanically activated TRAAK have different biophysical characteristics consistent with distinct channel open states. By varying applied pressure over approximately an hour of single channel records, we sampled a wide range of $TRAAK_{WT}$ activity ($0.01 \leq$ open probability (P_O) ≤ 0.98) (Fig. 1C–F, S1A,B, Table S1). We analyzed records in three

bins according to P_O (Fig. 1C). We found that in addition to a simple increase in P_O, mechanically activated TRAAK openings are distinct from basal openings in two ways.

First, mechanical force favors higher conductance openings (Figs. 1G–I, S2). Two conductance states are observed in $TRAAK_{WT}$ a low conductance opening with a unitary current of ~1 pA and a high conductance opening with a unitary current of ~2 pA. In unstretched patches at low P_O ($0.01 \leq P_O \leq 0.07$), the two conductance states are observed at roughly similar frequency (Fig. 1G,M). At intermediate P_O (mid P_O, $0.38 \leq P_O \leq 0.69$), more high conductance openings are observed (Fig. 1H,M). In records mechanically activated to high P_O ($0.93 \leq P_O \leq 0.98$), almost all openings are high conductance (Fig. 1I,M). Notably, unitary currents of these openings do not change significantly as a function of P_O, but the relative proportion of each conductance state does (Fig. 1G–J,M).

Second, mechanical force favors longer duration openings. Two kinetically distinct open states are observed in $TRAAK_{WT}$ records: a short duration (~1 ms) opening and a long duration (~3 ms or longer) opening (Figs. 1K, S3). In unstretched patches at low P_O, almost all openings are short duration (Fig. 1M). In contrast, when mechanically activated to high P_O, almost all openings are long duration. At intermediate P_O, both short and long duration openings are observed. Open duration and unitary current are positively correlated: low conductance openings have a narrow duration distribution around 1 ms while high conductance openings have a wider duration distribution ≥2 ms, with longer openings observed at higher P_O (Fig. 1M).

In addition, mechanical force favors shorter duration closures. $TRAAK_{WT}$ accesses two kinetically distinct closed states: a short duration (~0.5 ms) closure and a long duration (~3 ms or longer) closure (Figs. 1L, S4). Short duration closures of comparable length are observed in all records. However, long duration closures are only observed in low and intermediate P_O records and their prevalence and duration decrease as P_O increases (Figs. 1L, S3).

Single channel $TRAAK_{WT}$ records can be well fit with a simple linear kinetic model relating the two closed states (long duration (C1) and short duration (C2)) and two open states (short duration/low conductance (O1) and long duration/high conductance (O2)), though additional transitions between states are likely possible (Fig. 1N, Table S1)(Sorum et al., 2021). The distribution of states and the duration of C1 and O2 are dependent on membrane tension. When mechanically activated to high P_O, long duration closures and short duration/low conductance openings are almost never observed, so data can be fit with a two-state equilibrium model between C2 and O2 states (Figs. 1I,K–M, S2–4, Table S1). At intermediate P_O, the duration of long C1 closures is shorter than those at low P_O and the duration of O2 openings is shorter than those at high P_O (Figs. 1H, K–M, S2–4, Table S1). We conclude that mechanically activated openings correspond to the O2 state while basal openings correspond to the O1 state. We speculate weak mechanical activation by resting membrane tension in the patch results in low P_O O2 openings with a conductance distinct from O1 openings (Brohawn et al., 2014b; Opsahl and Webb, 1994). However, the duration of O1 and O2 openings at low P_O is similarly short and therefore indistinguishable kinetically (Fig. 1D,K).

We then asked whether we could identify the structural basis for these two distinct TRAAK open states. We reasoned that gain-of-function mutations could differentially stabilize particular open states and investigated three point mutants reported to dramatically increase channel activity: $TRAAK_{A198E}$, $TRAAK_{A270P}$, and $TRAAK_{G158D}$. $TRAAK_{A198E}$ and $TRAAK_{A270P}$ were recently identified in human patients with the neurological and developmental disorder FHEIG while $TRAAK_{G158D}$ was identified as a pan-K2P gain-of-function mutation (Bauer et al., 2018; Ben Soussia et al., 2019).

Mechanical force and FHEIG mutations promote a TM4 up open state

We first consider the FHEIG mutations $TRAAK_{A198E}$ and $TRAAK_{A270P}$ (Figs. 2A, 3A). Macroscopic recordings of $TRAAK_{A198E}$ or $TRAAK_{A270P}$ channels display currents that are only subtly activated by mechanical force, consistent with the initial characterization of these mutations (Figs. 2B,C, 3B,C) (Bauer et al., 2018). These recordings are representative of the maximum level of channel activation observed before patch rupture (Figure S5A–C). Single channel records reveal a simple explanation for reduced mechanical activation of $TRAAK_{A198E}$ and $TRAAK_{A270P}$ relative to $TRAAK_{WT}$. $TRAAK_{A198E}$ and $TRAAK_{A270P}$ open probability is nearly one at rest and mechanical force does not change channel conductance, so stimulation can only slightly increase channel activity (Figs. 2D–G, 3D–G, S1C,D).

$TRAAK_{A198E}$ and $TRAAK_{A270P}$ single channel behavior closely matches $TRAAK_{WT}$ when mechanically activated to high P_O. $TRAAK_{A198E}$ and $TRAAK_{A270P}$ openings are nearly all high conductance (with a unitary current ~2 pA) and long duration (~3 ms or longer), while closures are short duration (~0.5 ms) (Figs. 2F–J, 3F–J). The modest mechanical activation of $TRAAK_{A198E}$ and $TRAAK_{A270P}$ is due to an increase in long duration openings without significantly changing closed duration.

We determined crystal structures of $TRAAK_{A198E}$ and $TRAAK_{A270P}$ in the presence of K^+ and in complex with a mouse monoclonal antibody Fab fragment (Figs. 2A, 3A, S6A–F, Table S2). Data were anisotropic and extended along the three crystallographic axes to 2.3, 2.4, and 3.3 Å resolution for $TRAAK_{A198E}$ and 2.7, 2.9, and 3.9 Å resolution for $TRAAK_{A270P}$. As previously reported for this crystal form (Brohawn et al., 2013, 2014b), the conformation of one side of the TRAAK dimer is restricted because it is involved in forming contacts that propagate the lattice (Fig. S6G,H). We therefore focus our discussion on the opposing side of the TRAAK dimer (including TM4 from protomer B), which is conformationally unrestricted. In the same crystallization conditions, $TRAAK_{WT}$ adopts a TM4 down nonconductive conformation; the membrane-facing lateral opening above TM4 permits hydrophobic acyl chains to access the channel cavity and block ion passage (Fig. 2K) (Brohawn et al., 2014b). $TRAAK_{A198E}$ and $TRAAK_{A270P}$, however, adopt TM4 up conformations (Figs. 2L, 3K). Movement of TM4 up seals the membrane-facing lateral openings, preventing acyl chain access to the cavity and creating an unobstructed path for ion movement through the channel. This TM4 up conformation is similar to a $TRAAK_{WT}$ TM4 up conductive conformation captured in the presence of a small molecule activator trichloroethanol (overall r.m.s.d = 0.2 Å between $TRAAK_{A198E}$ or $TRAAK_{A270P}$ and $TRAAK_{WT}$ (PDB 4WFE), Fig. S7A,B,E) (Brohawn et al., 2014b). As observed in the

$TRAAK_{WT}$ TM4 up conductive structure, density consistent with a K^+ ion is present in the cavities of $TRAAK_{A198E}$ and $TRAAK_{A270P}$ (Figs. 3L, S6I).

To confirm that the $TRAAK_{A198E}$ TM4 up structure represents an open state, we determined a second structure in the presence of Tl^+ (to 2.8, 2.8, and 3.8 Å resolution along the three crystallographic axes, Table S2) and used anomalous diffraction of Tl^+ ions to unambiguously identify ion binding sites. Indeed, a Tl^+ ion is identified in the channel cavity in addition to four sites in the selectivity filter (S1-S4) and one on the extracellular mouth of the pore (S0), consistent with a conductive conformation (Fig. 2M).

How do $TRAAK_{A198E}$ and $TRAAK_{A270P}$ promote TM4 up open states? Comparing $TRAAK_{A198E}$ and $TRAAK_{WT}$ suggests two mechanisms in this mutant (Fig. 2N). The first is a steric relay from A198E through F201 and Y271 that favors TM4 up. In $TRAAK_{WT}$, the TM4 down conformation involves movement of Y271 1 ~ towards the cytoplasm relative to TM4 up. This requires the intracellular TM2-TM3 linkage to rotate 15° away from TM4 to prevent a clash between Y271 on TM4 and F201 on TM3. In $TRAAK_{A198E}$, TM2-TM3 is similarly rotated out, but A198E pushes F201 closer to TM4 where it would clash with Y271 in a TM4 down conformation. A second possibility is that A198E causes local thinning of the lipid bilayer to favor TM4 up. While A198 is predicted to be embedded in the membrane inner leaflet facing hydrophobic residues on TM4 down, the negatively charged carboxylic acid of A198E likely favors hydration of this pocket, promoting TM4 up to maintain nonpolar interactions between its hydrophobic residues and lipid acyl chains (Brooks, B. R. and Brooks, III, C. L. and Mackerell, Jr. et al., 2009; Jo et al., 2008). Analysis of two additional mutants at this position are consistent with both mechanisms contributing to channel activation, with charge playing a larger role. A smaller negatively charged residue in $TRAAK_{A198D}$ activates the channel to a similar degree as $TRAAK_{A198E}$ based on maximum observed mechanical stimulation (Fig. S5E–G). In contrast, a bulky uncharged residue in $TRAAK_{A198W}$ still activates the channel relative to wild-type, but approximately two-fold less than $TRAAK_{A198E}$ (Fig. S5A,E–G).

Comparing $TRAAK_{A270P}$ and $TRAAK_{WT}$ provides a structural explanation for channel activation: a proline at position 270 produces a kink in TM4 that closely approximates the $TRAAK_{WT}$ TM4 up conformation (Fig 3M). In $TRAAK_{WT}$, movement of TM4 up depends on a hinge at a conserved glycine G268. The A270P mutation instead disrupts backbone hydrogen bonding in TM4 to create a ~27° bend and ~9.5 Å upward movement of TM4 relative to $TRAAK_{WT}$ TM4 down.

We conclude that the $TRAAK_{A198E}$, $TRAAK_{A270P}$ and $TRAAK_{WT}$ TM4 up structures correspond to the high conductance/long duration mechanically activated open state O2. The following lines of evidence support this assignment: (i) $TRAAK_{A198E}$ and $TRAAK_{A270P}$ have an open probability ≤ 0.9 (Figs. 2F,H; 3F,H), (ii) the structures are similar to a $TRAAK_{WT}$ mechanically activated conductive conformation (Figs. 2K,L; 3K), (iii) the structures show unobstructed conduction paths with ions in the channel cavities (Figs. 2M, 3L, S6I), (iv) the predominant $TRAAK_{A198E}$ and $TRAAK_{A270P}$ unitary current is indistinguishable from $TRAAK_{WT}$ O2 (Figs. 1I, 2G, 3G), and (v) the mean duration of

the $TRAAK_{A198E}$ and $TRAAK_{A270P}$ open states are indistinguishable from $TRAAK_{WT}$ O2 (Figs. 1K, 2I, 3I, S3).

A TM4 down open state promoted by a pan-K2P activating mutation underlies basal activity

We next consider $TRAAK_{G158D}$ (Fig. 4A). In macroscopic recordings, mechanical force activates $TRAAK_{G158D}$ a maximum of ~2-fold; more than $TRAAK_{A198E}$ and $TRAAK_{A270P}$, but less than $TRAAK_{WT}$(Fig. 4B–D, S5A–D). We note that recordings and quantification of mechanical activation in macroscopic patches (Fig. 1A,B; 2B,C; 3B,C; 4B–D) correspond to maximum mechanical activation observed prior to membrane rupture. Pressure values required for maximal activation vary between patches and are not directly comparable (Fig. S5A–D) due to variation in patch geometry that results in different relationships between applied pressure and membrane tension generated that opens the channel (Moe and Blount, 2005). Single channel analysis shows that, similar to $TRAAK_{WT}$, mechanical activation of $TRAAK_{G158D}$ involves an increase in both open probability and conductance (Fig. 4E–H, S1E–I). However, the resting open probability of $TRAAK_{G158D}$ (P_O ~0.7) is much higher than $TRAAK_{WT}$ (P_O ~0.04) so mechanical stimulation of $TRAAK_{G158D}$ has a correspondingly smaller maximum effect (Fig. 4E,F). Basal openings of $TRAAK_{G158D}$ are low conductance with a unitary current ~1 pA while mechanically activated openings are higher conductance with a unitary current ~2 pA (Figs. 4G–I, S2).

Kinetic analysis shows that $TRAAK_{G158D}$ closely resembles $TRAAK_{WT}$ except that the long duration closed state C1 is absent in the mutant (Figs. 4J, S3, S4). $TRAAK_{G158D}$ accesses only a single short closed state (Fig. 4K). Like $TRAAK_{WT}$, $TRAAK_{G158D}$ has two open states, one short duration/low conductance (~1 ms / 1 pA) and one long duration/high conductance (~3 ms or longer / 2 pA) (Fig. 4I,J). Mechanical stimulation favors longer duration/high conductance openings. (Figs. 4L, S2, S3).

We determined the crystal structure of $TRAAK_{G158D}$ (to 2.9, 3.1, and 3.7 Å resolution along the three crystallographic axes) in the presence of K^+ (Fig. 4A, Table S2). $TRAAK_{G158D}$ adopts a TM4 down conformation like $TRAAK_{WT}$ crystallized under the same conditions (overall r.m.s.d = 0.2 Å between $TRAAK_{G158D}$ and $TRAAK_{WT}$ (PDB 4WFE))(Fig. 4M). However, spherical shaped density in the $TRAAK_{G158D}$ cavity is consistent with a K^+ ion rather than the hydrophobic acyl chain present in the $TRAAK_{WT}$ TM4 down structure (Fig. 4N). Attempts to use Tl^+ anomalous diffraction to unambiguously determine the identity of the spherical shaped density in the $TRAAK_{G158D}$ cavity were inconclusive due to limited size of $TRAAK_{G158D}$ crystals grown in Tl^+ and correspondingly weak overall anomalous signal. However, the shape of the cavity density and high resting open probability of the mutant channel (P_O ~0.7) are most consistent with the $TRAAK_{G158D}$ structure representing a TM4 down open state.

$TRAAK_{G158D}$ likely promotes a TM4 down open state through a simple electrostatic consequence of the mutation (Fig. 4O, a comparison to $TRAAK_{WT}$ is shown in Fig. S7M–P). G158D projects into the channel cavity ~5 Å underneath the selectivity filter and increases hydrophilicity of the ion conduction path close to where acyl chains are observed in nonconductive TM4 down $TRAAK_{WT}$ structure. The electronegative cavity

of $TRAAK_{G158D}$ is expected to disfavor acyl chain access and channel block, instead promoting ion occupancy in the cavity and a conductive open state. The increased cavity polarity may contribute to the observed difference in voltage-dependance between $TRAAK_{WT}$ and $TRAAK_{G158D}$ (Fig. 1A,B; 4B,C).

We conclude that the TM4 down open state captured in the $TRAAK_{G158D}$ structure corresponds to the low conductance/short duration basal open state O1 in $TRAAK_{WT}$. The following data support this assignment: (i) $TRAAK_{G158D}$ has a high resting open probability (Fig. 4E), (ii) a K^+ ion rather than an acyl chain is observed in the $TRAAK_{G158D}$ cavity (Fig. 4N), (iii) unitary current of the $TRAAK_{G158D}$ basal open state is indistinguishable from $TRAAK_{WT}$ O1 (Fig. 4I), (iv) mean dwell time of the $TRAAK_{G158D}$ short duration opening is statistically indistinguishable from $TRAAK_{WT}$ O1 (Fig. 4J), and (v) like $TRAAK_{WT}$, the basal low conductance/short duration $TRAAK_{G158D}$ O1-like open state can be mechanically activated to a high conductance/long duration O2-like open state (Fig. 4F–J). Consistent with (v), $TRAAK_{G158D}$ can adopt a TM4 up-like conformation (observed on the side of the channel involved in forming crystal contacts) and $TRAAK_{G158D}$ TM4 up is expected to be energetically favored in the presence of membrane tension relative to $TRAAK_{G158D}$ TM4 down because it has an increased cross-sectional area (Brohawn et al., 2014b) (Fig. S7C). The energetic difference between TM4 down and TM4 up states may be different in the mutant; trichloroethanol has no effect on $TRAAK_{G158D}$ current in whole cell recordings under conditions that activate $TRAAK_{WT}$ (Fig. S5H–J).

We further conclude that the TM4 down lipid-blocked closed state observed in the $TRAAK_{WT}$ structures corresponds to the long duration closed state C1. Analogous long duration closures are not observed in in $TRAAK_{G158D}$, $TRAAKA_{A198E}$, or $TRAAK_{A270P}$ (Figs. 1L, 2J, 3J, 4K). In $TRAAK_{A198E}$ and $TRAAK_{A270P}$, this is likely because TM4s are favored in an up conformation that seals lateral membrane openings, preventing lipid access to the cavity (Figs. 2L, 3K). In $TRAAK_{G158D}$, this is likely because the mutation increases polarity of the channel cavity to disfavor occupancy of hydrophobic acyl chains (Fig. 4O).

Discussion

Together, these data support a model for TRAAK gating shown in Figure 5 that maps structural conformations to a linear four-state kinetic model derived from single-channel records (Fig. 1N). Long duration closures (C1) correspond to the TM4 down, lipid blocked conformation captured in $TRAAK_{WT}$ structures (Brohawn et al., 2014b). Low conductance/short duration basal openings (O1) correspond to the TM4 down, conductive conformation captured in the $TRAAK_{G158D}$ structure (Fig. 4). High conductance/long duration mechanically activated openings (O2) correspond to the TM4 up, conductive conformation captured in structures of $TRAAK_{A198E}$, $TRAAK_{A270P}$, and $TRAAK_{WT}$ with activating small molecules (Fig. 2,3). Structures of two other gain-of-function mutations, $TRAAK_{G124I}$ and $TRAAK_{W262S}$, have been previously reported (Lolicato et al., 2014), although their open probability, single channel behavior, and cavity ion occupancy is not known. However, both adopt TM4 down-like conformations and may promote O1 like openings similarly to $TRAAK_{G158D}$.

$TRAAK_{WT}$ under basal conditions transitions primarily between C1, O1, and C2 states. The channel predominantly adopts a lipid-blocked TM4 down closed state C1, but spontaneous delipidation in the absence of protein conformational changes results in short O1 openings until lipid rebinding. These O1 openings underlie basal activity. Mechanical force favors the TM4 up open state O2 because it involves shape changes (relative to TM4 down) that are energetically favored in the presence of membrane tension, including an increase in cross-sectional area and cylindricity(Brohawn et al., 2014b). Mechanical force disfavors the TM4 down states C1 and O1 because the relatively smaller cross-sectional area and more wedge-shaped structure is disfavored in the presence of membrane tension. Higher membrane tension increasingly favors promotes and stabilizes TM4 up, resulting in longer duration O2 openings and correspondingly shorter duration C1 closures.

The gain of function mutations $TRAAK_{A198E}$ and $TRAAK_{A270P}$ mimic mechanically activated $TRAAK_{WT}$ by promoting a TM4 up conductive conformation. As a consequence, $TRAAK_{A198E}$ and $TRAAK_{A270P}$, like mechanically activated $TRAAK_{WT}$, primarily transition between O2 and C2 states. Gain of function mutant $TRAAK_{G158D}$ mimics basally open $TRAAK_{WT}$, promoting a conductive TM4 down conformation by disfavoring lipid entry and channel block at low membrane tension. As a consequence, $TRAAK_{G158D}$ primarily transitions between O1, C2, and O2 states. Like $TRAAK_{WT}$, mechanical stimulation of $TRAAK_{G158D}$ disfavors O1 to favor transitions between O2 and C2 states.

Differences in the chemical and geometric properties of the conduction path likely explain differences in properties of basal O1 and mechanically-activated O2 openings. The cavity diameter is larger and more polar near the cytoplasmic entrance to the channel in the TM4 up O2 open state compared to a TM4 down O1 open state (Fig. S7M–P). These differences are expected to result in lower access resistance to the cavity, which would explain the higher conductance of O2 compared to O1 openings.

The short duration closure (C2) does not yet have a defined structural correlate. We observe C2-like closures of similar duration in all TRAAK variants analyzed (Figs. 1L, 2J, 3J, 4K), suggesting they may occur independently of TM4 position or cavity environment. One possibility is that C2 closures represent gating at the selectivity filter. While gating conformational changes at the selectivity filter have not been observed in TRAAK, they have been hypothesized from functional data and visualized in other K2Ps including the mechanosensitive TREK1 in low $[K^+]$ and pH-gated TASK2 in physiological $[K^+]$ and low pH (Li et al., 2020; Lolicato et al., 2020). Alternatively, C2 closures could correspond to cavity dewetting that has been proposed to occur based on molecular dynamics simulations (Aryal et al., 2014, 2015) or other, yet to be visualized, conformational rearrangements.

Notably, some evidence suggests that the physical basis for distinct modes of TRAAK activity shown here could be shared among K2P channels. Differences between basal and stimulus-activated openings, including their kinetics and voltage dependence (Schewe et al., 2016), have been reported for other K2Ps, suggesting that physically distinct open states could similarly underlie different modes of channel activity (Bang et al., 2000; Gnatenco et al., 2002; Kang et al., 2005; Maingret et al., 1999; Sorum et al., 2021). Mutations analogous to $TRAAK_{G158D}$ were found to activate all K2P channels, with the extent of

activation correlated with the polarity of the introduced amino acid change (Ben Soussia et al., 2019). Membrane-facing openings have been observed in TM4-down-like structures of TREK2 (Dong et al., 2015), TWIK1 (Miller and Long, 2012), TASK1 (Rödström et al., 2020), and TASK2 (Li et al., 2020) in addition to TRAAK (Brohawn et al., 2012) (Fig. S7D–L). Acyl chains that could block conduction were modeled in TWIK1, TREK2, and TRAAK structures (Brohawn et al., 2012; Dong et al., 2015; Miller and Long, 2012), though their absence in other K2Ps may be due to limited resolution of, or partial occupancy in, structures determined to date. This raises the possibility that lipid-mediated block could be more common among K2Ps than currently appreciated. Like TRAAK, basal activity of other K2Ps could result from transient unbinding of lipid from channel cavities and ion passage through an unobstructed conduction path, while stimulus gating could involve conformational changes that prevent lipid entry into the channel entirely (Brohawn et al., 2012, 2014b; Dong et al., 2015; Li et al., 2020; Miller and Long, 2012; Rödström et al., 2020).

STAR Methods

Resource availability

Lead contact—Further information and requests for resources and reagents should be directed to and will be fulfilled by the lead contact, Stephen Brohawn (sbrohawn@berkeley.edu).

Materials availability—Plasmids used in this study are available upon request.

Data and code availability—Single channel analysis code written in Python for this paper is available on Github: (https://github.com/BrohawnLab/ElectrophysiologyScripts/tree/singles0).

The X-ray crystallographic coordinates and structure factors for $TRAAK_{A198E}$ in K^+ (7LJ5), $TRAAK_{A198E}$ in Tl^+ (7LJA), $TRAAK_{A270P}$ in K^+ (7LJ4), and $TRAAK_{G158D}$ (7LJB) are available at the Protein Data Bank.

Experimental model and subject details

Cell lines—Oocytes were harvested from female *Xenopus laevis* frogs obtained from Nasco and housed at the University of Califoirnia, Berkeley in the Office for Animal Care and Use (OLAC) facilities. The use of oocytes was approved by the Animal Use and Care Committee at the University of California, Berkeley under AUP-2019-11-12743.

Method details

Electrophysiology—Full length hsTRAAK (Uniprot Q9NYG8-2) was codon optimized for eukaryotic expression, synthesized (Genewiz), and cloned into a modified pGEMHE vector using XhoI and EcoRI restriction sites such that the mRNA transcript encodes hsTRAAK 1-419 with an additional “SNS” at the C-terminus. Point mutants G158D, A198E, and A270P were generated by inverse PCR of the parent construct and verified by Sanger sequencing. cRNA was transcribed from linearized plasmids *in vitro* using T7

polymerase, and 0.1–10 ng cRNA was injected into *Xenopus laevis* oocytes extracted from anaesthetized frogs.

Currents were recorded at 25°C from inside-out patches excised from oocytes 1–5 days after mRNA injection. Pipette solution contained (in mM) 15 KCl, 135NaCl, 2$MgCl_2$, 10 HEPES, pH = 7.4 with NaOH. The solution in the bath contained 150 KCl, 2 $MgCl_2$, 10 HEPES, 1 EGTA, pH = 7.1 with KOH. All single channel records were made at a holding voltage of 0 mV and presented in physiological convention.

Currents were recorded using an Axopatch 200B Patch Clamp amplifier at a bandwidth of 1 kHz and digitized with an Axon Digidata 1550B at 50 to 500 kHz. To maintain the integrity of brief TRAAK dwell times, records were not further filtered unless explicitly stated. Baseline correction was performed manually based on the observable closed state for each recording; since there was no solution exchange in our experiments, no associated large drifts in baseline were observed. Portions of $TRAAK_{WT}$ records were assigned as low, mid, or high P_O for analysis. Low P_O was observed prior to pressure application, while mid and high P_O behavior was observed after pressure application. Portions of mutant records during pressure application were analyzed separately from mutant records prior to pressure application. High $P_O$$TRAAK_{WT}$ and mutant records with pressure were made with the highest achievable pressure prior to patch rupture. Single channel open-close transitions were idealized by half-amplitude threshold crossing and dwell time event lists were generated for each baseline corrected record. Dwell time histograms were generated from the dwell time event lists using custom built software (Sorum et al., 2015), while the fits for these histograms were generated in GraphPad Prism version 9.0 using single, double, or triple Gaussian fits.

For unitary current analysis, event lists for $TRAAK_{WT}$ low P_O, $TRAAK_{WT}$ mid P_O, $TRAAK_{G158D}$, and $TRAAK_{G158D}$ with pressure were first generated in Clampfit 10.7, applying a 0.8 pA event detection cutoff. Currents were filtered to 10 kHz and were analyzed with a custom script in Python 3.7 using the pyABF module (Harden, 2019). Each point in the filtered record was annotated as closed (C1/C2), open low conductance (O1), or open high conductance (O2) using the events list. To account for the sharp detection cutoff, openings were padded by an additional point on either side of the cutoff (these points corresponded to 100 us of ~0.5-1 pA current during openings and closings). Open only event lists were then generated by removing all closed points. Open event only lists were binned by 0.2 pA in current and 0.2 ms in time to generate bubble plots relating unitary current and mean open duration for $TRAAK_{WT}$ and $TRAAK_{G158D}$. Open only event lists were also used to generate open event current histograms to distinguish relatively rare low conductance openings from prevalent closed events. Mean unitary currents for $TRAAK_{WT}$ low P_O and $TRAAK_{WT}$ mid P_O were derived from Gaussian fits to these open event current histograms. Mean unitary currents for $TRAAK_{WT}$ high P_O and all mutants were derived from Gaussian fits to square root total event current histograms in order to distinguish conductance states when one state is present at higher frequency.

For TEVC recordings, the bath was ND96 with or without 5 mM trichloroethanol. Pipettes were filled 3M KCl and had resistances of 0.5-2 MΩ. Currents induced by voltage steps

were first recorded in ND96 bath solution. Next, half the bath solution was removed and replaced by the same volume of ND96 with trichloroethanol to ensure the bath volume remained constant between recordings.

Protein expression and purification—Human TRAAK (UniProt Q9NYG8-2) was cloned for expression in *Pichia pastoris* cells as previously described (Brohawn et al., 2012) with modifications described here. The construct used for purification included an additional 26 amino acid N-terminal sequence compared to Q9NYG8-1 that improved heterologous expression. The final construct is C-terminally truncated by 119 amino acids, incorporates two mutations to remove N-linked glycosylation sites (N104Q/N108Q), and is expressed as a C-terminal PreScission protease-cleavable EGFP-10xHis fusion protein. As a result, there is an additional amino acid sequence of “SNSLEVLFQ” at the C-terminus of the final purified protein after protease cleavage. Recombinant *Pichia* were grown in a 4 liter fermenter and harvested 48-72h after induction with methanol.

30-120g of frozen *Pichia* cells expressing TRAAK were disrupted by milling (Retsch model MM301) 5 times for 3 minutes at 25 Hz. All subsequent purification steps were carried out at 4 °C. Milled cells were resuspended in buffer A (in mM) 50 Tris pH 8.0, 150 KCl, 1 EDTA 0.1 mg/mL DNase1, 1 mg/mL pepstatin, 1 mg/mL leupeptin, 1 mg/mL aprotinin, 10 mg/mL soy trypsin inhibitor, 1 mM benzamidine, 100 μM AEBSF, 1 μM E-64, and 1 mM phenylmethysulfonyl fluoride added immediately before use) at a ratio of 1 g cell pellet per 4 mL lysis buffer and sonicated for 16 minutes with a duty cycle of 15 seconds of sonication per minute. The solution was ultracentrifuged at 150,000 xg for 1 hour at 4 °C. Pellets were transferred to a Dounce homogenizer in buffer B (buffer A + 60 mM DM). Following homogenization, solutions were stirred for 3 hours at 4 °C followed by centrifugation at 33,000g for 45 minutes. Anti-GFP nanobody resin (1 mg purified anti-GFP nanobody conjugated to 1 mL resin) was washed in Buffer B and added to the supernatant at a ratio of 1 mL resin / 15 g *Pichia* cells. The solution was gently stirred for 3 hours. Resin was collected on a column and washed in 15 column volumes (CV) of Buffer C (buffer A +6 mM DM+ 150 mM KCl), followed by 2 CV Buffer D (buffer A +6 mM DM). The resin was resuspended in ~3 CV of Buffer D with 1 mg purified Precission protease and gently rocked in column overnight. Cleaved TRAAK was eluted in ~4 CV of Buffer D, concentrated (50 kDa MWCO), and applied to a Superdex 200 SEC column (GE Healthcare) equilibrated in Buffer E (20 mM Tris pH 8.0, 150 mM KCl, 1 mM EDTA, 4 mM DM). Peak fractions were pooled and concentrated to 200-300 μL for incubation with Fab 13E9 and subsequently applied to a Superdex 200 column (GE Healthcare) equilibrated in Buffer E. Fab 13E9 was prepared as described previously(Brohawn et al., 2014b). TRAAK-Fab complexes were pooled and concentrated to 25-33 mg/mL for hanging drop crystallization. For crystallization in Tl^+, all purification steps were conduction as with KCl, with two exceptions: KCl is substituted for KNO_3 for all buffers except Buffer E, where KCl is substituted with $TlNO_3$.

Protein Crystallization—Crystals were grown in drops of 0.125–0.250 μL protein added to an equal volume of reservoir, in hanging drops over a 100 μL reservoir at 4 °C. Reservoir for each mutant in KCl was 50mM Tris pH 8.8, 64-200 mM $CaCl_2$, 27–33%

(vol/vol) PEG400. Reservoir for each mutant in $TINO_3$ was 50 mM Tris pH 8.8, 64-200 mM $Ca(NO3)_2$, 27–33%(vol/vol)PEG400. Lower Calcium concentrations were observed to correspond to increased nucleation and rapid growth of large, well-ordered crystals. Crystals grew to ~100 μm x 100 μm x 200 μm in 1–5 weeks. TRAAK A270P crystals rarely achieved sizes larger than 70 μm x 70 μm x 100 μm after 5 weeks.

For cryoprotection, an approximately equal volume of mother liquor supplemented to be 30%(vol/vol) PEG400 was added to one side of the drop and crystals were moved through this solution with a cryoloop before being plunged into liquid nitrogen.

X-ray Data Collection, Model Building & Refinement—Data were collected at beamline 8.3.1 at the ALS, or 24-IDC & 24-IDE at the APS. Thallium-containing crystals were collected at 12680 eV, and Potassium-containing crystals were collected at 12663 eV. Were rotated 360 degrees, and data were collected in 0.20 degree wedges with a 0.25 second exposure time per wedge. Datasets were processed as individual wedges in XDS (Kabsch, 2010; Kabsch et al., 2010). Some datasets were truncated to eliminate redundant data displaying beam-induced damage prior to scaling with XSCALE, and merging with XDSCONV (Kabsch et al., 2010). Due to the anisotropy of the data, elliptically truncated resolution cutoffs generated by STARANISO (Tickle et al., 2018) were used to increased overall resolution of the maps. Structures were solved by molecular replacement using Phaser (McCoy et al., 2007) with an input model of nonconductive hsTRAAK for G158D (PDB ID 4WFF) and conductive hsTRAAK for A198E and A270P mutants (PDB ID 4WFE). Structure refinement was carried out in Coot (Emsley and Cowtan, 2004) and Refmac5 (Murshudov et al., 2011). Jelly body and automatically generated local NCS constraints were used throughout refinement. For the final round of refinement, three TLS groups per protein chain were incorporated. Molprobity was used to assess model geometry in later stages of refinement (Chen et al., 2010).

Ion occupancy in the conduction axis was determined by calculating either a model phased anomalous difference map for A198E crystals grown in Thallium, or a Polder map for G158D and A270P crystals grown Potassium. In all maps, density in the filter fits well to ions occupying the S1, 2, 3, and 4 positions. Similarly, densities above the filter (S0) are well fit with one or two ions. Density in the cavity below the filter is also fit with an ion. All ion occupancies are set to 1.

The angle and orientation of transmembrane helix 4 in each model was compared using UCSF Chimera (Pettersen et al., 2004). Cross-sectional area calculations were performed with CHARMM (Brooks, B. R. and Brooks, III, C. L. and Mackerell, Jr. et al., 2009; Jo et al., 2007, 2008). The area calculation used a surface calculated with 1.4 Å added to the van der Waals radii of protein atoms, and a probe radius of 3.5 Å to approximate lipid-accessible surface area. A water cylinder with a 6 Å radius was used to fill the cavity of TRAAK channels to exclude its contribution from the calculation. All calculations are made with channels containing symmetric protomers of the B chain, which does not make a contact in the crystal. Symmetric molecules were generated by rotation of the B protomer about the conduction axis, using pore helix and selectivity filter residues 119-133 and 228-242. Pore radii and pore-lining residue hydropathy were calculated with CHAP (Klesse et al., 2019)

using a pathway lining residue margin value of 0.55 and a hydrophobicity kernel bandwidth of 0.45.

Quantification and statistical analysis

Data analysis was performed using Excel (Microsoft) Prism 9.1 (GraphPad). Statistical details are described in the Results, Figures, and Figure Legends. All data are mean ± SEM. Exact values of n are reported where appropriate. Depending on the experiment, n represents number of patches, number of cells, or number of crystals.

Supplementary Material

Refer to Web version on PubMed Central for supplementary material.

Acknowledgements

We thank R. MacKinnon for the 13E9 anti-human TRAAK hybridoma cell line. We thank staff at ALS beamline 8.3.1, especially J. Holton and G. Meigs, and at APS beamline 24-IDC/E, especially I. Kourinov, for assistance at the synchrotron. We thank all members of the Brohawn laboratory for discussions. SGB is a New York Stem Cell Foundation-Robertson Neuroscience Investigator. This work was supported by the New York Stem Cell Foundation, NIGMS grant DP2GM123496, a McKnight Foundation Scholar Award, a Klingenstein-Simons Foundation Fellowship Award, a Sloan Research Fellowship, and a Rose Hill Innovator Award to SGB.

References

Aryal P, Abd-Wahab F, Bucci G, Sansom MSP, and Tucker SJ (2014). A hydrophobic barrier deep within the inner pore of the TWIK-1 K2P potassium channel. Nat. Commun

Aryal P, Sansom MSP, and Tucker SJ (2015). Hydrophobic gating in ion channels. J. Mol. Biol

Bagriantsev SN, Peyronnet R, Clark KA, Honoré E, and Minor DL (2011). Multiple modalities converge on a common gate to control K2P channel function. EMBO J.

Bang H, Kim Y, and Kim D (2000). TREK-2, a new member of the mechanosensitive tandem-pore K+ channel family. J. Biol. Chem

Barel O, Shalev SA, Ofir R, Cohen A, Zlotogora J, Shorer Z, Mazor G, Finer G, Khateeb S, Zilberberg N, et al. (2008). Maternally Inherited Birk Barel Mental Retardation Dysmorphism Syndrome Caused by a Mutation in the Genomically Imprinted Potassium Channel KCNK9. Am. J. Hum. Genet

Bauer CK, Calligari P, Radio FC, Caputo V, Dentici ML, Falah N, High F, Pantaleoni F, Barresi S, Ciolfi A, et al. (2018). Mutations in KCNK4 that Affect Gating Cause a Recognizable Neurodevelopmental Syndrome. Am. J. Hum. Genet

Brohawn SG, del Marmol J, and MacKinnon R (2012). Crystal Structure of the Human K2P TRAAK, a Lipid-and Mechano-Sensitive K+ Ion Channel. Science (80-.). 335, 436–441.

Brohawn SG, Campbell EB, and MacKinnon R (2013). Domain-swapped chain connectivity and gated membrane access in a Fab-mediated crystal of the human TRAAK K+ channel. Proc. Natl. Acad. Sci. U. S. A

Brohawn SG, Su Z, and MacKinnon R (2014a). Mechanosensitivity is mediated directly by the lipid membrane in TRAAK and TREK1 K+ channels. Proc. Natl. Acad. Sci. U. S. A 111, 3614–3619. [PubMed: 24550493]

Brohawn SG, Campbell EB, and MacKinnon R (2014b). Physical mechanism for gating and mechanosensitivity of the human TRAAK K+ channel. Nature 516, 126–130. [PubMed: 25471887]

Brohawn SG, Wang W, Handler A, Campbell EB, Schwarz JR, and MacKinnon R (2019). The mechanosensitive ion channel traak is localized to the mammalian node of ranvier. Elife.

Brooks BR and Brooks CL III and Mackerell AD Jr. and, Nilsson L and Petrella RJ and Roux B and Won Y and A. G and Bartels C and Boresch S and Caflisch A and Caves L and, Cui Q and Dinner AR and Feig M and Fischer S and Gao J and, Hodoscek M and Im W and Kuczera K and Lazaridis T and Ma J, and Ovchinnikov V and Paci E and Pastor RW and Post CB and, Pu JZ and Schaefer M and Tidor B and Venable RM and, and Woodcock HL and Wu X and Yang W and York DM and Karplus M (2009). CHARMM: The Biomolecular Simulation Program. J. Comput. Chem

Chatelain FC, Bichet D, Douguet D, Feliciangeli S, Bendahhou S, Reichold M, Warth R, Barhanin J, and Lesage F (2012). TWIK1, a unique background channel with variable ion selectivity. Proc. Natl. Acad. Sci. U. S. A

Chen VB, Arendall WB, Headd JJ, Keedy DA, Immormino RM, Kapral GJ, Murray LW, Richardson JS, and Richardson DC (2010). MolProbity: All-atom structure validation for macromolecular crystallography. Acta Crystallogr. Sect. D Biol. Crystallogr

Cohen A, Ben-Abu Y, Hen S, and Zilberberg N (2008). A novel mechanism for human K2P2.1 channel gating: Facilitation of C-type gating by protonation of extracellular histidine residues. J. Biol. Chem

Dong YY, Pike ACWW, Mackenzie A, McClenaghan C, Aryal P, Dong L, Quigley A, Grieben M, Goubin S, Mukhopadhyay S, et al. (2015). K2P channel gating mechanisms revealed by structures of TREK-2 and a complex with Prozac. Science (80-.). 347, 1256–1259.

Emsley P, and Cowtan K (2004). Coot: Model-building tools for molecular graphics. Acta Crystallogr. Sect. D Biol. Crystallogr

Enyedi P, and Czirják G (2010). Molecular background of leak K+ currents: two-pore domain potassium channels. Physiol. Rev 90, 559–605. [PubMed: 20393194]

Gnatenco C, Han J, Snyder AK, and Kim D (2002). Functional expression of TREK-2 K+ channel in cultured rat brain astrocytes. Brain Res.

Harden S (2019). Analysis of electrophysiological recordings was performed with custom software written for this project using Python 3.7 and the pyABF module.

Heurteaux C, Lucas G, Guy N, El Yacoubi M, Thümmler S, Peng XD, Noble F, Blondeau N, Widmann C, Borsotto M, et al. (2006). Deletion of the background potassium channel TREK-1 results in a depression-resistant phenotype. Nat. Neurosci

Jo S, Kim T, and Im W (2007). Automated builder and database of protein/membrane complexes for molecular dynamics simulations. PLoS One.

Jo S, Kim T, Iyer VG, and Im W (2008). CHARMM-GUI: A web-based graphical user interface for CHARMM. J. Comput. Chem

Kabsch W (2010). Integration, scaling, space-group assignment and post-refinement. Acta Crystallogr. Sect. D Biol. Crystallogr

Kabsch W, T. BA, K. D, A. KP, K. D, S. M, G. RRB, P. E, S. F, K. W, et al. (2010). XDS.. Acta Crystallogr. Sect. D Biol. Crystallogr

Kanda H, Ling J, Tonomura S, Noguchi K, Matalon S, and Gu JG (2019). TREK-1 and TRAAK Are Principal K+ Channels at the Nodes of Ranvier for Rapid Action Potential Conduction on Mammalian Myelinated Afferent Nerves. Neuron.

Kang D, Choe C, and Kim D (2005). Thermosensitivity of the two-pore domain K + channels TREK-2 and TRAAK. J Physiol 5641, 103–116.

Klesse G, Rao S, Sansom MSP, and Tucker SJ (2019). CHAP: A Versatile Tool for the Structural and Functional Annotation of Ion Channel Pores. J. Mol. Biol

Lafrenière RG, Cader MZ, Poulin JF, Andres-Enguix I, Simoneau M, Gupta N, Boisvert K, Lafrenière F, McLaughlan S, Dubé MP, et al. (2010). A dominant-negative mutation in the TRESK potassium channel is linked to familial migraine with aura. Nat. Med

Li B, Rietmeijer RA, and Brohawn SG (2020). Structural basis for pH gating of the two-pore domain K+ channel TASK2. Nature.

Lolicato M, Riegelhaupt PM, Arrigoni C, Clark KA, and Minor DL (2014). Transmembrane helix straightening and buckling underlies activation of mechanosensitive and thermosensitive K<inf>2P</inf> channels. Neuron 84, 1198–1212. [PubMed: 25500157]

Lolicato M, Natale AM, Abderemane-Ali F, Crottès D, Capponi S, Duman R, Wagner A, Rosenberg JM, Grabe M, and Minor DL (2020). K2Pchannel C-type gating involves asymmetric selectivity filter order-disorder transitions. Sci. Adv

Ma L, Roman-Campos D, Austin ED, Eyries M, Sampson KS, Soubrier F, Germain M, Tregouët DA, Borczuk A, Rosenzweig EB, et al. (2013). A novel channelopathy in pulmonary arterial hypertension. N. Engl. J. Med.

Maingret F, Fosset M, Lesage F, Lazdunski M, and Honoré E (1999). TRAAK is a mammalian neuronal mechano-gated K+ channel. J. Biol. Chem 274, 1381–1387. [PubMed: 9880510]

McClenaghan C, Schewe M, Aryal P, Carpenter EP, Baukrowitz T, and Tucker SJ (2016). Polymodal activation of the TREK-2 K2P channel produces structurally distinct open states. J. Gen. Physiol 147, 497–505. [PubMed: 27241700]

McCoy AJ, Grosse-Kunstleve RW, Adams PD, Winn MD, Storoni LC, and Read RJ (2007). Phaser crystallographic software. J. Appl. Crystallogr

Miller AN, and Long SB (2012). Crystal structure of the human two-pore domain potassium channel K2P1. Science 335, 432–436. [PubMed: 22282804]

Moe P, and Blount P (2005). Assessment of potential stimuli for mechano-dependent gating of MscL: Effects of pressure, tension, and lipid headgroups. Biochemistry 44, 12239–12244. [PubMed: 16142922]

Murshudov GN, Skubák P, Lebedev AA, Pannu NS, Steiner RA, Nicholls RA, Winn MD, Long F, and Vagin AA (2011). REFMAC5 for the refinement of macromolecular crystal structures. Acta Crystallogr. Sect. D Biol. Crystallogr

Niemeyer MI, Cid LP, Peña-Münzenmayer G, and Sepúlveda FV (2010). Separate gating mechanisms mediate the regulation of K2P potassium channel TASK-2 by intra- and extracellular pH. J. Biol. Chem

Noël J, Zimmermann K, Busserolles J, Deval E, Alloui A, Diochot S, Guy N, Borsotto M, Reeh P, Eschalier A, et al. (2009). The mechano-activated K± channels TRAAK and TREK-1 control both warm and cold perception. EMBO J.

Opsahl LR, and Webb WW (1994). Lipid-glass adhesion in giga-sealed patch-clamped membranes. Biophys J 66, 75–79. [PubMed: 8130347]

Patel AJ, Honoré E, Maingret F, Lesage F, Fink M, Duprat F, and Lazdunski M (1998). A mammalian two pore domain mechano-gated S-like K+ channel. EMBO J.

Pettersen EF, Goddard TD, Huang CC, Couch GS, Greenblatt DM, Meng EC, and Ferrin TE (2004). UCSF Chimera - A visualization system for exploratory research and analysis. J. Comput. Chem

Piechotta PL, Rapedius M, Stansfeld PJ, Bollepalli MK, Erhlich G, Andres-Enguix I, Fritzenschaft H, Decher N, Sansom MSP, Tucker SJ, et al. (2011). The pore structure and gating mechanism of K2P channels. EMBO J.

Renigunta V, Schlichthörl G, and Daut J (2015). Much more than a leak: Structure and function of K2P-channels. Pflugers Arch. Eur. J. Physiol 867–894. [PubMed: 25791628]

Rödström KEJ, Kiper AK, Zhang W, Rinné S, Pike ACW, Goldstein M, Conrad LJ, Delbeck M, Hahn MG, Meier H, et al. (2020). A lower X-gate in TASK channels traps inhibitors within the vestibule. Nature.

Royal P, Andres-Bilbe A, Ávalos Prado P, Verkest C, Wdziekonski B, Schaub S, Baron A, Lesage F, Gasull X, Levitz J, et al. (2019). Migraine-Associated TRESK Mutations Increase Neuronal Excitability through Alternative Translation Initiation and Inhibition of TREK. Neuron.

Sandoz G, Douguet D, Chatelain F, Lazdunski M, and Lesage F (2009). Extracellular acidification exerts opposite actions on TREK1 and TREK2 potassium channels via a single conserved histidine residue. Proc. Natl. Acad. Sci. U. S. A

Schewe M, Nematian-Ardestani E, Sun H, Musinszki M, Cordeiro S, Bucci G, De Groot BL, Tucker SJ, Rapedius M, and Baukrowitz T (2016). A Non-canonical Voltage-Sensing Mechanism Controls Gating in K2P K+ Channels. Cell 164, 937–949. [PubMed: 26919430]

Schmidt C, Wiedmann F, Voigt N, Zhou XB, Heijman J, Lang S, Albert V, Kallenberger S, Ruhparwar A, Szabó G, et al. (2015). Upregulation of K2P 3.1 K + Current Causes Action Potential Shortening in Patients with Chronic Atrial Fibrillation. Circulation.

Sorum B, Czégé D, and Csanády L (2015). Timing of CFTR Pore Opening and Structure of Its Transition State. Cell.

Sorum B, Rietmeijer RA, Gopakumar K, Adesnik H, and Brohawn SG (2021). Ultrasound activates mechanosensitive TRAAK K+ channels through the lipid membrane. Proc. Natl. Acad. Sci. U. S. A.

Ben Soussia I, El Mouridi S, Kang D, Leclercq-Blondel A, Khoubza L, Tardy P, Zariohi N, Gendrel M, Lesage F, Kim EJ, et al. (2019). Mutation of a single residue promotes gating of vertebrate and invertebrate two-pore domain potassium channels. Nat. Commun

Tickle IJ, Flensburg C, Keller P, Paciorek W, Sharff A, Vonrhein C, and Bricogne G (2018). STARANISO. Cambridge, United Kingdom Glob. Phasing Ltd..

Vierra NC, Dadi PK, Jeong I, Dickerson M, Powell DR, and Jacobson DA (2015). Type 2 diabetes-associated K+ channel TALK-1 modulates β-cell electrical excitability, second-phase insulin secretion, and glucose homeostasis. Diabetes.

Xian Tao Li, Dyachenko V, Zuzarte M, Putzke C, Preisig-Müller R, Isenberg G, and Daut J (2006). The stretch-activated potassium channel TREK-1 in rat cardiac ventricular muscle. Cardiovasc. Res

Highlights

- The K2P TRAAK has physically distinct leak and mechanically-activated open states
- FHEIG syndrome causing mutations promote mechanically-activated openings
- A pan-K2P activating mutation in the channel cavity promotes leak openings
- Leak openings occur with TM4 down and mechanically-activated openings with TM4 up

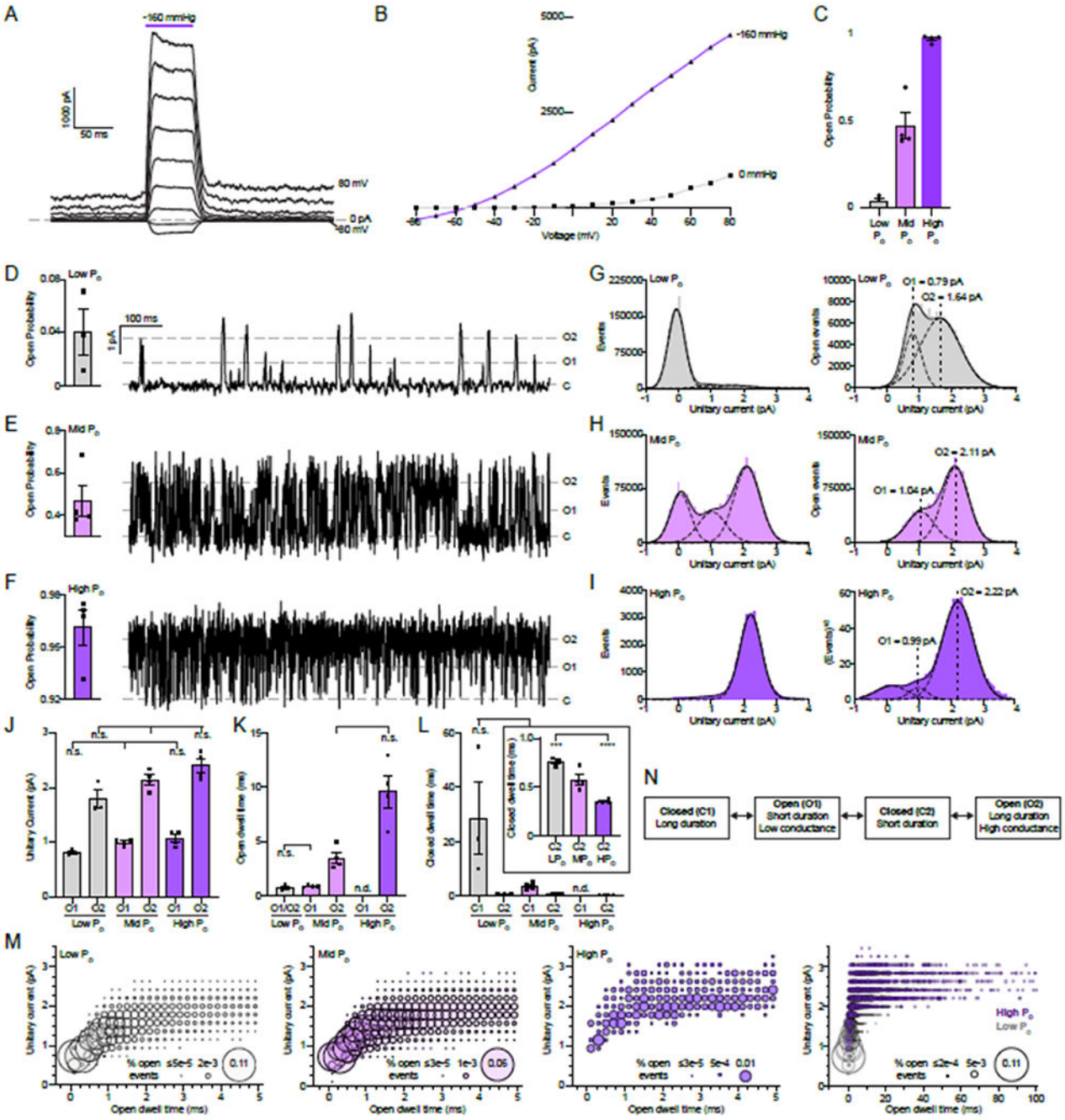

Figure 1 –. Distinct basal and mechanically-activated open states in TRAAK$_{WT}$.

(A) Macroscopic currents recorded across an inside-out patch pulled from a TRAAK-expressing cell in response to a voltage step protocol (V_{hold} = 0, V_{test} = −80 to 80, ΔV = 10 mV, 20 mV intervals displayed) with a pressure step applied at each voltage (purple bar). (B) Current-voltage relationship from (A). (C) Open probability calculated from single channel records (0.04 ± 0.02, 0.47 ± 0.07, and 0.96 ± 0.01 for low P_O, mid P_O, and high P_O, respectively (mean ± sem, n = 3, 4, and 4 patches)). All single channel data in the paper were recorded at V_{hold} = 0 mV in a ten-fold gradient of [K^+] and are presented in

physiological convention. (D-F) 1 s portion from representative low P_O, mid P_O, and high P_O recordings, respectively. (G-I) All event (left) and open-only or square root all event (right) current histograms from representative low P_O, mid P_O, and high P_O recordings, respectively. (J) Unitary currents of O1 and O2 states (0.81 ± 0.03 pA and 1.80 ± 0.16 pA, 0.99 ± 0.03 pA and 2.14 ± 0.09 pA, and 1.07 ± 0.07 pA and 2.41 ± 0.13 pA for low P_O, mid P_O, and high P_O recordings, respectively (mean ± sem, n= 3, 4, and 4 patches)). (K) Open dwell time of O1 and O2 states (0.80 ± 0.15 ms, 0.91 ± 0.05 ms and 3.52 ± 0.51 ms, and 9.60 ± 1.46 ms for low P_O, mid P_O, and high P_O recordings, respectively (mean ± sem, n= 3, 4, and 4 patches)). (L) Closed dwell times of C1 and C2 states (28.70 ± 13.50 and 0.77 ± 0.03 ms, 3.59 ± 0.67 and 0.58 ± 0.05 ms, and 0.35 ± 0.01 ms for low P_O, mid P_O, and high P_O recordings, respectively (mean ± sem, n=3, 4, and 4 patches, n.d. not determined, n.s. not significant, ***p = 0.0006, ****p < 0.0001 (one-way ANOVA with Tukey correction)). (M) Unitary current-open dwell time relationships for low P_O, mid P_O, and high P_O open events and an overlay of low P_O and high P_O relationships at expanded time scale. Bubble size is proportional to percentage of open events. (N) Four state TRAAK gating model. See also Figures S1–5, Table S1.

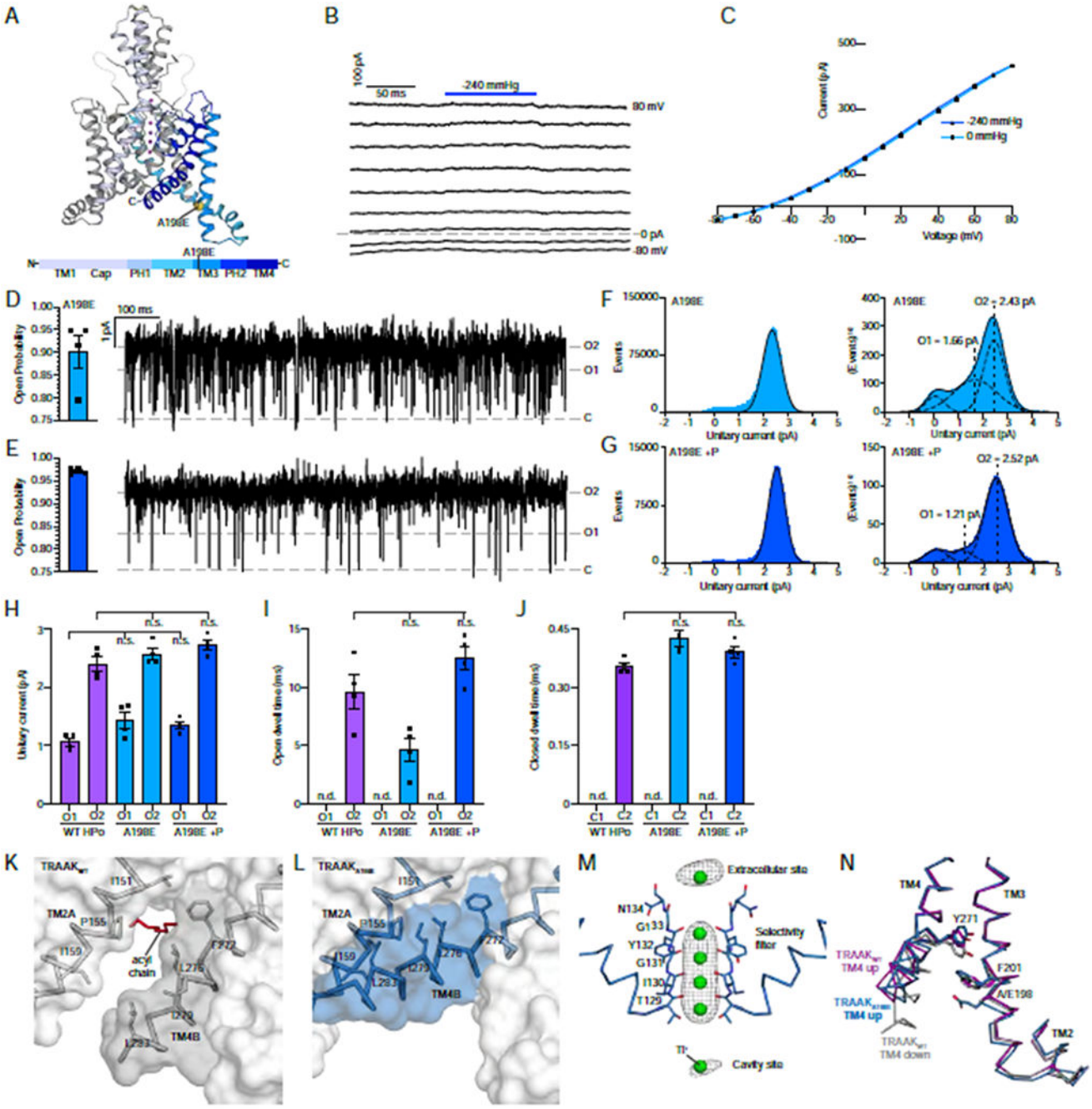

Figure 2 –. The FHEIG mutation TRAAK$_{A198E}$ promotes a long duration, high conductance TM4-up open state.

(A) Crystal structure of TRAAK$_{A198E}$. Side view from the membrane plane with one protomer gray and the second protomer colored according to the key below. A198E is shown as a yellow sphere and K^+ ions are colored purple. (B) Macroscopic currents from a TRAAK$_{A198E}$-containing patch in response to a voltage step protocol (V_{hold} = 0, V_{test} = −80 to 80, ΔV = 10 mV, 20 mV intervals displayed) with a pressure step applied at each voltage (dark blue bar). (C) Current-voltage relationship from (B). (D,E) Open probability calculated from all TRAAK$_{A198E}$ and TRAAK$_{A198E}$ with pressure (+P) records

(left, P_O = 0.90 ± 0.04 and P_O = 0.97 ± 0.003 (mean ± sem, n = 4 patches) and 1 s portion from representative recordings. (F,G) All event (left) and square root all event (right) current histograms from representative recordings. (H) Unitary currents of $TRAAK_{WT}$ HP_O, $TRAAK_{A198E}$, and $TRAAK_{A198E}$+P O1 and O2 states (1.07 ± 0.07 and 2.41 ± 0.13 pA, 1.44 ± 0.14 and 2.57 ± 0.10 pA, and 1.35 ± 0.06 and 2.72 ± 0.09 pA, respectively). (I) Open dwell times of $TRAAK_{WT}$ HP_O, $TRAAK_{A198E}$, and $TRAAK_{A198E}$+P O2 states (9.60 ± 1.46 ms, 4.63 ±1.03 ms, 12.46 ±1.02 ms, respectively). (J) Closed dwell times of $TRAAK_{WT}$ HP_O, $TRAAK_{A198E}$, and $TRAAK_{A198E}$+P C2 (0.35 ± 0.01 ms, 0.42 ± 0.02 ms, and 0.39 ± 0.01 ms, respectively). For H-J, data are mean ± sem, n = 4 patches; n.d., not determined; n.s., not significant (one-way Anova with Dunnett correction). (K) View of the membrane-facing lateral opening in a $TRAAK_{WT}$ TM4-down structure (PDB 4WFF). A cavity-bound lipid acyl chain blocks conduction. (L) $TRAAK_{A198E}$ in the same view as (K). A TM4-up conformation seals the membrane opening. (M) Ions in a $TRAAK_{A198E}$-Tl^+ structure. Anomalous density (grey) around Tl^+ ions (green) displayed at 2.5 σ (extracellular / selectivity filter / cavity ions). (N) Overlay of the TM2-TM3-TM4 interaction from $TRAAK_{A198E}$ and $TRAAK_{WT}$ structures. A198E sterically promotes a TM4-up open state. See also Figures S1–7, Tables S1,S2.

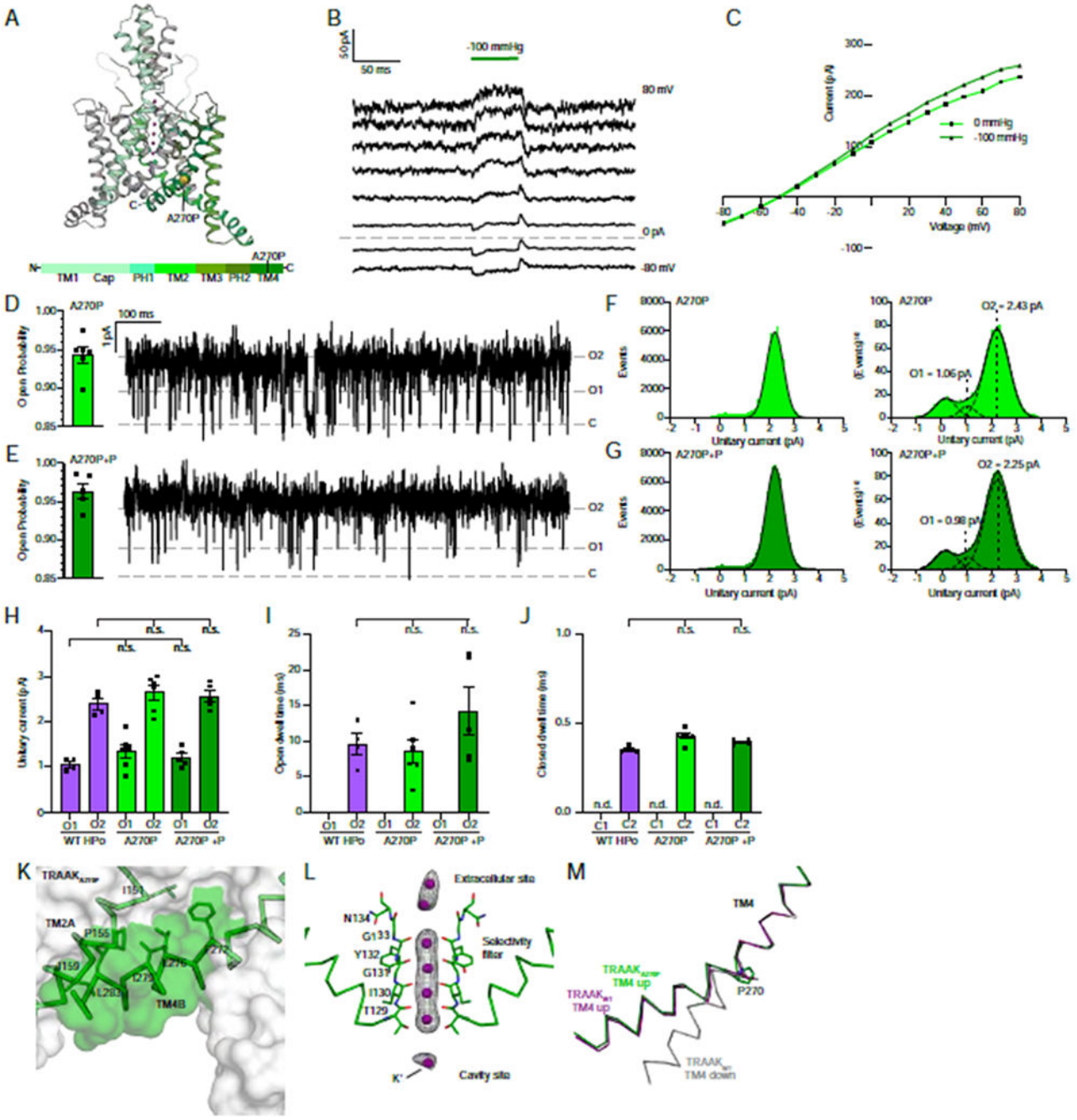

Figure 3 –. The FHEIG mutation TRAAK$_{A270P}$ promotes a long duration, high conductance TM4-up open state.

(A) Crystal structure of TRAAK$_{A270P}$. Side view from the membrane plane with one protomer gray and the second protomer colored according to the key below. A270P is shown as a yellow sphere and K^+ ions are colored purple. (B) Macroscopic currents from a TRAAK$_{A270P}$-containing patch in response to a voltage step protocol (V_{hold} = 0, V_{test} = −80 to 80, ΔV = 10 mV, 20 mV intervals displayed) with a pressure step applied at each voltage (dark green bar). (C) Current-voltage relationship from (B). (D,E) Open probability calculated from all TRAAK$_{A270P}$ and TRAAK$_{A270P}$ with pressure (+P) records

(left, P_O = 0.94 ± 0.01 and P_O = 0.96 ± 0.01 (mean ± sem, n = 6 and 5 patches) and 1 s portion from representative recordings. (F,G) All event (left) and square root all event (right) current histograms from representative recordings. (H) Unitary currents of $TRAAK_{WT}$ HP_O, $TRAAK_{A270P}$, and $TRAAK_{A270P}$+P O1 and O2 states (1.07 ± 0.07 and 2.41 ± 0.13 pA, 1.34 ± 0.15 and 2.65 ± 0.16 pA, and 1.21 ± 0.09 and 2.57 ± 0.12 pA, respectively). (I) Open dwell times of $TRAAK_{WT}$ HP_O, $TRAAK_{A270P}$, and $TRAAK_{A270P}$+P O2 states (9.60 ± 1.46 ms, 8.56 ± 1.69 ms, and 14.47 ± 3.30 ms, respectively). (J) Closed dwell times of $TRAAK_{WT}$ HP_O, $TRAAK_{A270P}$, and $TRAAK_{A270P}$+P C2 (0.35 ± 0.01 ms, 0.43 ± 0.01 ms, and 0.39 ± 0.01 ms, respectively). For H-J, data are mean ± sem, n = 4, 6, and 5 patches; n.d., not determined; n.s., not significant (one-way Anova with Dunnett correction). (K) View of the membrane-facing cytoplasmic half of TM4 in $TRAAK_{A270P}$. A TM4-up conformation seals the membrane opening. (L) Ions in the $TRAAK_{A270P}$-K^+ structure. Polder omit F_o-F_c density (grey) around K^+ ions (purple) displayed at 5 and 5.5 σ for extracellular and selectivity filter and cavity ions, respectively. (M) Overlay of TM4 from $TRAAK_{A270P}$ and $TRAAK_{WT}$ structures. A270P kinks TM4 to promote a TM4-up open state. See also Figures S1–7, Tables S1,S2.

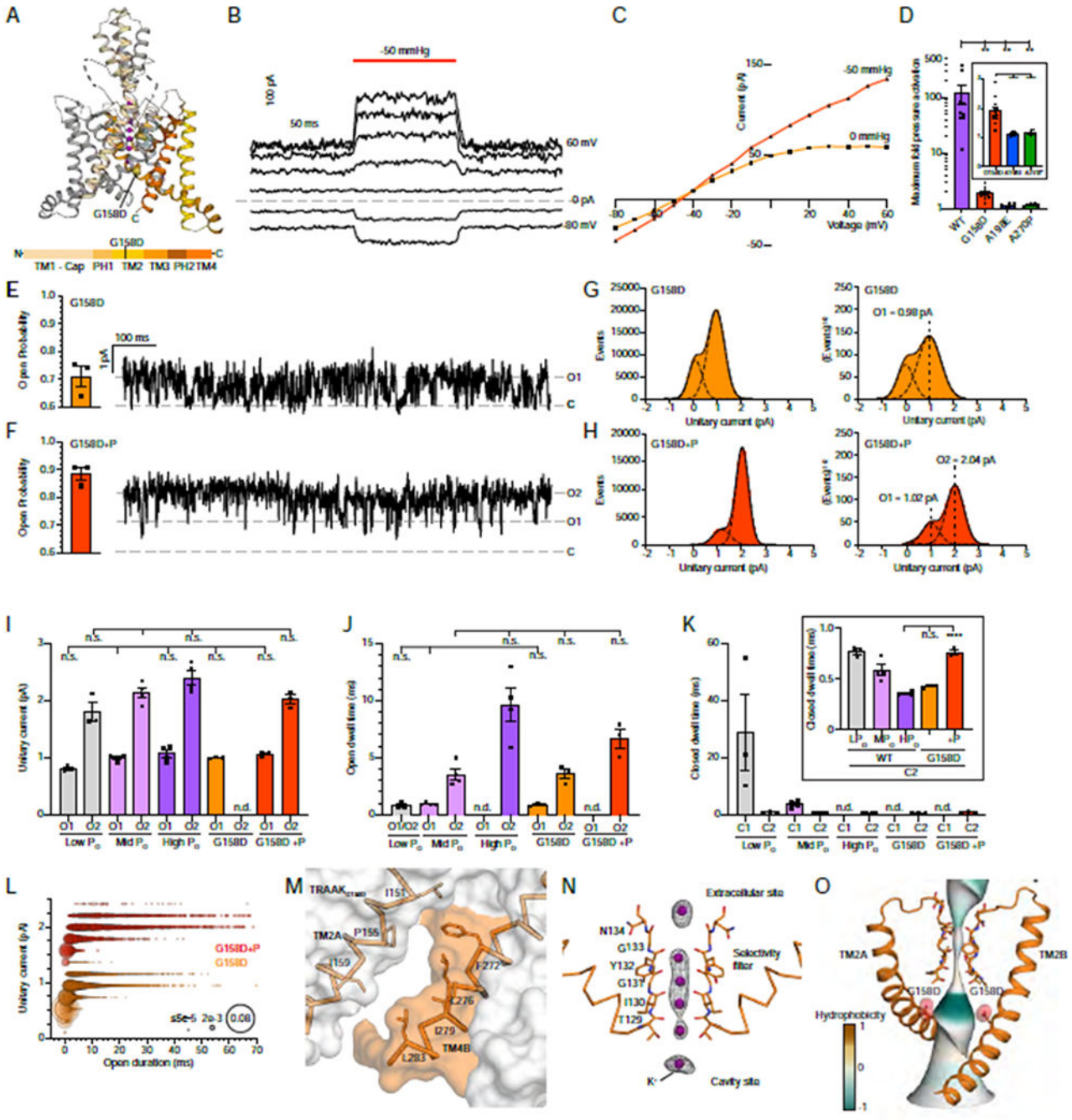

Figure 4 –. The gain-of-function mutation TRAAK$_{G158D}$ promotes a short duration, low conductance TM4-down open state.

(A) Crystal structure of TRAAK$_{G158D}$. Side view from the membrane plane with one protomer gray and the second protomer colored according to the key below. G158D is shown as a yellow sphere and K^+ ions are colored purple. (B) Macroscopic currents from a TRAAK$_{G158D}$-containing patch in response to a voltage step protocol (V_{hold} = 0, V_{test} = −80 to 80, ΔV = 10 mV, 20 mV intervals displayed) with a pressure step applied at each voltage (dark orange bar). (C) Current-voltage relationship from (B). (D) Maximum fold-activation by pressure of macroscopic TRAAK$_{WT}$, TRAAK$_{G158D}$, TRAAK$_{A198E}$, and TRAAK$_{A270P}$

currents with expanded scale in inset (119.8 ± 45.38, 1.91 ± 0.14, 1.12 ± 0.02, and 1.16 ± 0.02, respectively, mean ± sem, n = 9, 11, 7, and 8, **p < 0.0021, ****p < 0.0001 (one-way ANOVA with Dunnett correction). (E,F) Open probability calculated from all $TRAAK_{G158D}$ and $TRAAK_{G158D}$ with pressure (+P) records (left, P_O = 0.71 ± 0.04 and P_O= 0.89 ± 0.02 (mean ± sem, n=3 patches) and 1s portion from representative recordings. (G,H) All event (left) and square root all event (right) current histograms from representative recordings. (I) Unitary currents of $TRAAK_{WT}$ LP_O, MP_O, HP_O, $TRAAK_{G158D}$, and $TRAAK_{G158D}$+P O1 and O2 states (0.81 ± 0.03 pA and 1.80 ± 0.16 pA, 0.99 ± 0.03 pA and 2.14 ± 0.09 pA, 1.07 ± 0.07 pA and 2.41 ± 0.13 pA, 0.99 ± 0.01, and 1.06 ± 0.02 and 2.02 ± 0.08 pA, respectively). (J) Open dwell times of $TRAAK_{WT}$ LP_O, MP_O, HP_O, $TRAAK_{G158D}$, and $TRAAK_{G158D}$+P O1and O2 states (0.80 ± 0.15 ms, 0.91 ± 0.05 ms and 3.52 ± 0.51 ms, 9.60 ± 1.46 ms, 0.88 ± 0.07 and 3.58 ± 0.46 ms, and 6.63 ± 0.83 ms, respectively). (K) Closed dwell times of $TRAAK_{WT}$ LP_O, MP_O, HP_O, $TRAAK_{G158D}$, and $TRAAK_{G158D}$+P C1 and C2 states (28.70 ± 13.50 and 0.77 ± 0.03 ms, 3.59 ± 0.67 and 0.58 ± 0.05 ms, 0.35 ± 0.01 ms, 0.42 ± 0.01 ms, and 0.76 ± 0.03 ms, respectively). For I-K, data are mean ± sem, n = 3, 4, 4, 3 and 3 patches; n.d., not determined; n.s., not significant, ****p < 0.0001 (one-way Anova with Tukey correction). (L) Unitary current-open dwell time relationships for $TRAAK_{G158D}$, and $TRAAK_{G158D}$+P open events and an overlay at expanded time scale. Bubble size is proportional to percentage of open events. (M) View of the membrane-facing cytoplasmic half of TM4 in $TRAAK_{G158D}$. (N) Ions in the $TRAAK_{G158D}$-K^+ structure. Polder omit F_o-F_c density (grey) around K^+ ions (purple) displayed at 6.5 and 6 σ for selectivity filter and extracellular and cavity ions, respectively. (O) The conduction path in $TRAAK_{G158D}$ colored by hydrophobicity. G158D increases cavity electronegativity to promote a TM4-down open state. See also Figures S1–7, Tables S1,S2.

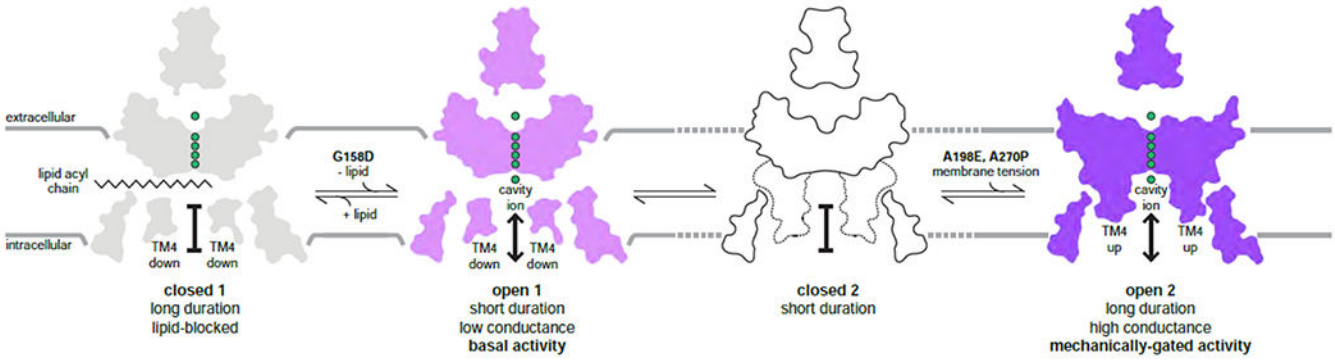

Figure 5 –. An integrated model for TRAAK gating with distinct basal and mechanically-gated open states.

Known structures are mapped to the linear-four state model for TRAAK gating. Basal activity corresponds to a TM4-down, low conductance, short duration open state O1. Mechanically-gated activity corresponds to a TM4-up, high conductance, long duration open state O2. Long duration closures correspond to a TM4-down lipid-blocked state C1. The unknown structure of the short duration closed state C2 is drawn without ions and the position of TM4 is indicated with dashed lines.

KEY RESOURCES TABLE

REAGENT or RESOURCE	SOURCE	IDENTIFIER
Bacterial and virus strains		
STABL2	ThermoFisher	CAT#10268019
Chemicals, peptides, and recombinant proteins		
DM (Sol-Grade)	Anatrace	CAT#D322S
DM (Analytical Grade)	Anatrace	CAT#D322
pepstatin	Gold Biotechnology	CAT#P-020
leupeptin	Gold Biotechnology	CAT#L-010
aprotinin	Gold Biotechnology	CAT#A-655
soy trypsin inhibitor	Gold Biotechnology	CAT#T9128
benzamidine	Gold Biotechnology	CAT#B-6506
AEBSF	Gold Biotechnology	CAT#A-540
E-64	Gold Biotechnology	CAT#E-064
phenylmethysulfonyl fluoride	Gold Biotechnology	CAT#P-470
CNBr-conjugated sepharose	Cytiva	CAT#17043001
Critical commercial assays		
mMessage machine T7 transcription kit	ThermoFisher	CAT#AM1344
Deposited data		
TRAAK A198E-13E9 Fab complex in K+	This paper	7LJ5
TRAAK A198E-13E9 Fab complex in Tl+	This paper	7LJA
TRAAK A270P-13E9 Fab complex in K+	This paper	7LJ4
TRAAK G158D-13E9 Fab complex in K+	This paper	7LJB
Experimental models: Cell lines		
13E9 antibody hydriboma	Brohawn 2014	gift from R. Mackinnon, Rockefeller University
Xenopus laevis oocytes	This paper	N/A
Pichia pastoris SMD1163 (Alternative SMD1168)	ThermoFisher	CAT#C17500
Experimental models: Organisms/strains		
Xenopus laevis	Nasco	CAT#LM00531
Oligonucleotides		
G158D_Fwd: GATATCTTGTTGGCTGGA	this paper	N/A
G158D_Rev: GAAGAGAGGGATACCAAC	this paper	N/A
A198E_Fwd: GAAATGCTGTTCCTCCTCATC	this paper	N/A
A198E_Rev: GGACAGTACACGAACCAA	this paper	N/A
A270P_Fwd: CCTTACTTCGCTAGTGTGCTC	this paper	N/A
A270P_Rev: CAGTCCCAACAGAATCC	this paper	N/A

REAGENT or RESOURCE	SOURCE	IDENTIFIER
A198D_Fwd: CGTGTACTGTCCGATATGCTGTTC	this paper	N/A
A198D_Rev: GAGGAGGAACAGCATATCGGA	this paper	N/A
A198W_Fwd: CGTGTACTGTCCTGGATGCTGTTC	this paper	N/A
A198W_Rev: GAGGAGGAACAGCATCCAGGA	this paper	N/A
Recombinant DNA		
TRAAK pPICz vector	Brohawn et. al, 2012	N/A
TRAAK PGEM vector	Sorum et. al, 2021	N/A
Software and algorithms		
Graphpad Prism Software	GraphPad Prism Software, Inc.	N/A
Excel	Microsoft, Inc.	https://www.microsoft.com/en-us/microsoft-365/excel
XDS	Kabsch et al. 2010	https://xds.mr.mpg.de/
STARANISO	Tickle et al. 2018	http://staraniso.globalphasing.org/
Refmac5	Murshudov et al., 2011	N/A
UCSF Chimera	Pettersen et al., 2004	https://www.cgl.ucsf.edu/chimera/
Coot	Emsley et al. 2010	https://www2.mrc-lmb.cam.ac.uk/personal/pemsley/coot
MolProbity	Chen et al. 2010	http://molprobity.biochem.duke.edu/
PyMol	Schrödinger, LLC	https://pymol.org/2/support.html#page-top
HOLE	Smart et al 1996	http://www.holeprogram.org/
CHAP	Kleese et al 2019	https://www.channotation.org/
CHARMM	Brooks et al., 2009; Jo et al., 2007, 2008	https://www.charmm-gui.org/
Python v3.6	Python	https://www.python.org
Python scripts for single channel event unitary current calculation, unitary current and dwell time 2D histogram calculation	This paper	https://github.com/sbrohawn/ElectrophysiologyScripts/tree/singles
Antibodies		
Anti-GFP nanobody	Addgene	CAT#61838